

## Space-time structure of long ocean swell fields

Matthias T. Delpey,<sup>1</sup> Fabrice Ardhuin,<sup>1</sup> Fabrice Collard,<sup>2</sup> and Bertrand Chapron<sup>3</sup>

Received 7 October 2009; revised 3 May 2010; accepted 31 August 2010; published 16 December 2010.

[1] The space-time structure of long-period ocean swell fields is investigated, with particular attention given to features in the direction orthogonal to the propagation direction. This study combines space-borne synthetic aperture radar (SAR) data with numerical model hindcasts and time series recorded by in situ instruments. In each data set the swell field is defined by a common storm source. The correlation of swell height time series is very high along a single great circle path with a time shift given by the deep water dispersion relation of the dominant swells. This correlation is also high for locations situated on different great circles in entire ocean basins. Given the Earth radius  $R$ , we define the distance from the source  $R\alpha$  and the transversal angle  $\beta$  so that  $\alpha$  and  $\beta$  would be equal the colatitude and longitude for a storm centered on the North Pole. Outside of land influence, the swell height field at time  $t$ ,  $H_{ss}(\alpha, \beta, t)$  is well approximated by a function  $H_{ss,0}(t - R\alpha/C_g)/\sqrt{(\alpha \sin(\alpha))}$  times another function  $r_2(\beta)$ , where  $C_g$  is a representative group speed. Here  $r_2(\beta)$  derived from SAR data is very broad, with a width at half the maximum that is larger than  $70^\circ$ , and varies significantly from storm to storm. Land shadows introduce further modifications so that in general  $r_2$  is a function of  $\beta$  and  $\alpha$ . This separation of variables and the smoothness of the  $H_{ss}$  field, allows the estimation of the full field of  $H_{ss}$  from sparse measurements, such as wave mode SAR data, combined with one time series, such as that provided by a single buoy. A first crude estimation of a synthetic  $H_{ss}$  field based on this principle already shows that swell hindcasts and forecasts can be improved by assimilating such synthetic observations.

**Citation:** Delpey, M. T., F. Ardhuin, F. Collard, and B. Chapron (2010), Space-time structure of long ocean swell fields, *J. Geophys. Res.*, 115, C12037, doi:10.1029/2009JC005885.

### 1. Introduction

[2] Sea states in large ocean basins are the result of the superposition of wave trains that propagate at different frequencies and directions. A wave train can be a locally generated wind sea and/or one swell field radiated from a distant storm [e.g., Gain, 1918; Barber and Ursell, 1948]. Long swells are generated by severe storms. During such events, the strongest winds are found in a well defined region, and for a limited time, typically of the order of 12 to 24 h. We call “swell field” the ensemble of swell trains that were all generated by this same meteorological event. This swell field may eventually cover a full ocean basin or more, and has a lifetime that can extend over a few weeks due to the swell propagation across ocean basins, sometimes more than 20,000 km from their source [Munk *et al.*, 1963].

[3] The first thorough investigation of swell was motivated by forecasting needs on the coast of Morocco during the colonial war of 1907–1912 [Gain, 1918]. The absence of

harbors was making the transportation of troops very difficult with unpredictable delays in ship offloading due to heavy swells, a concern soon shared by commercial shipping. Similar reasons, namely the amphibious landing of 1943, again on the coast of Morocco (before many further landings elsewhere), also produced a revival of interest in swell prediction in the 1940s [Sverdrup and Munk, 1947; Ursell, 1999]. The observed dispersive nature of swells also led to the implementation of the first spectral wave models, designed and implemented by Gelci *et al.* [1957] after a long experience with other methods of swell forecasting in Morocco [Gelci and Cazalé, 1953].

[4] Other investigations have complemented these North Atlantic studies, culminating with the work of Snodgrass *et al.* [1966] which essentially focused on the evolution of the swell energy along the propagation direction. That analysis of swell height was later refined by Gjevik *et al.* [1988] who investigated the effects of the motion of the source storm, and Ardhuin *et al.* [2009a] who provided accurate estimations of the dissipation rates of swell energy. All these studies essentially followed swells along a great circle and showed that it was possible to forecast swell heights at great distances. This method was pioneered by Montagne [1922] who used observations in the Azores to forecast swell heights in Morocco.

<sup>1</sup>Service Hydrographique et Oceanographique de la Marine, Brest, France.

<sup>2</sup>Division Radar, Collecte Localisation Satellites, Plouzane, France.

<sup>3</sup>Laboratoire d’Océanographie Spatiale, Ifremer, Plouzane, France.

[5] The development of ship and buoy networks, and the very important contribution of swell observation from satellite, has now revealed the consistency of swell parameters also in the transversal direction, on the scale of entire ocean basins, as shown by *Hasselmann et al.* [1996], *Voorrips et al.* [1997], or more recently by *Collard et al.* [2009].

[6] However, whereas the structure of frequency and direction in swell fields has been widely studied, the characteristics of the two-point space-time covariance of swell heights are essentially unexplored. In particular, the evolution of the energy distribution in the direction orthogonal to the propagation direction is not known. The correlation scales of the total significant wave height  $H_s$  has been investigated by *Tournadre* [1993], and *Greenslade and Young* [2005]. The latter study reveals a strong anisotropy of  $H_s$  in swell-dominated regions, with a maximum correlation scale in the direction perpendicular to dominant swell propagation directions. New assimilation techniques, that use swell partition information [e.g., *Voorrips et al.*, 1997; *Aouf et al.*, 2006a, 2006b], would benefit from similar studies of swell partition parameters.

[7] The goal of the present paper is thus to explore the correlation scales and structures of swell fields, in isolation from the rest of the sea state, with a view to provide information on the generating storms, and useful parameterization for the assimilation of swell-related measurements in numerical wave models. In particular we shall investigate the correlation in space and time, an effort dictated by the propagative nature of swells.

[8] First, in section 2, a short description of the data used in this study is presented. Then, in section 3, a simple and robust method for assembling swell fields from ensembles of swell partitions automatically generated from wave spectra is presented. The tracking is both applied to numerical wave model output and to measurements of wave buoys. Using this tracking method, a field can be isolated from the other fields and studied separately. The swell significant wave height ( $H_{ss}$ ) of such fields is then studied. The present work widely uses model results to reveal features of the structure of the  $H_{ss}$  field, which are subsequently validated by comparison with synthetic aperture radar (SAR) observations. The general properties of these features are presented in section 4 and used to generate similar  $H_{ss}$  fields using sparse SAR data, which provided comparable features as discussed in section 5. Finally, in section 6, a parameterization of the  $H_{ss}$  field is proposed and confronted to SAR observations. The conclusion and perspectives are summarized in section 7.

## 2. Data and Methods

### 2.1. Model Data

[9] Model results used in this paper are partitioned spectra computed by the wave model WAVEWATCH III™ (hereinafter WWATCH) using the version 3.14 [Tolman, 2008, 2009] with physical parameterization modified according to *Ardhuin et al.* [2009b] and corresponding to the TEST441 setup described by *Ardhuin et al.* [2010]. This parameterization includes, in particular, an explicit swell dissipation consistent with the observations of *Ardhuin et al.* [2009a]. It should be noted that the subgrid island blocking scheme of *Tolman* [2003] is used, as modified by *Tolman* [2007],

together with the third-order Ultimate Quickest propagation scheme including the correction for spurious effects of spectral discretization (the garden sprinkler effect), as proposed by *Tolman* [2002].

[10] The model was run on a  $0.5^\circ$  by  $0.5^\circ$  grid covering the entire ocean, with a local two-way nested zoom covering Tahiti and the Tuamotus at 10 times finer resolution. Computation outputs are given every 6 h. Output wave spectra are discretized over 32 frequencies exponentially spaced from 0.038 Hz to 0.72 Hz so that the bandwidth between two successive frequencies  $f_i$  and  $f_{i+1}$  is  $0.10f_i$ , and 24 directions with a constant  $15^\circ$  directional resolution. All model output fields are available at the URL <http://tinyurl.com/yetsofy>. WWATCH spectra are partitioned during run time using the method of *Hanson and Phillips* [2001], as described by *Tolman* [2009].

### 2.2. Buoy Data

[11] Buoy data used in this paper are partitioned wave spectra derived from the National Data Buoy Center (NDBC) platforms 51028 and 46029. Both wave measurement systems are pitch-and-roll 3 m diameter disc buoys, located on the Equator, off Christmas Island (Kiritimati), Kiribati ( $153.913^\circ\text{W}, 0^\circ\text{N}$ ), and off the Columbia River at the Oregon-Washington border ( $124.510^\circ\text{W}, 46.144^\circ\text{N}$ ). In order to make comparison easier with model spectra, buoy spectra are first averaged over 3 h and interpolated on the model frequency grid. This also allows a smoothing of the spectra that reduces noise effects.

[12] Buoy spectra are then partitioned using the method of *Gerling* [1992]. Although model spectra are partitioned using the (possibly) different method by *Hanson and Phillips* [2001], the two methods have been checked on model output and give equivalent results for our applications.

### 2.3. SAR Data

[13] The SAR data used in this paper are level 2 products provided by the European Space Agency (ESA) and collected during ENVISAT mission. These products are unambiguous wave directional spectra processed from SAR scenes using the method of *Chapron et al.* [2001], as updated by *Johnsen and Collard* [2004], with further bias corrections given by *Collard et al.* [2009]. The SAR data are partitioned using the method of *Gerling* [1992] after a smoothing procedure described by *Collard et al.* [2009].

## 3. Space-Time Tracking of Swell Fields

### 3.1. Space-Time Tracking Method

[14] To study the structure of a swell field, it is necessary to identify and isolate its contribution to the sea state. Spectral partitioning is the first step of this task. At a given observation point, a set of partitions of the ocean wave spectrum is defined. Each partition corresponds to the energetic contribution of a wave system [Gerling, 1992]. In order to associate swell partitions at different times and places to a common source, thus producing a field, *Voorrips et al.* [1997] proposed a cross-assignment tracking method based on the hypothesis of strong correlation between bulk parameters of two partitions related to the same swell field. To decide if two partitions are related to the same field or not, they used a set of empiric thresholds limiting the var-

iability of the energy and the (mean or peak) frequency and direction in neighboring points in space and time. With a different approach, *Aarnes and Krogstad* [2001] estimated a meteorological source event time and location from each partitions group. A group is then validated or refined by verifying that it corresponds to a unique generating event.

[15] In the present work, we exclusively use the uniqueness of the source to assemble the swell field. In our procedure, the time and location of the meteorological source are first estimated and this information is used to filter the swell partition data set. This procedure is well suited to our goal of defining clean or ideal swell fields, but it will naturally lead to gaps and thus is not applicable as such for a comprehensive assembly of the swell field. This approach may also select a specific type of swell field.

[16] Practically, a swell partition is accepted in the field if its peak frequency  $f_{ps}$  and its mean direction at the peak frequency  $\theta_{ps}$  are close enough to those given by linear wave theory applied to a point source, denoted  $(f_{ps,lin}, \theta_{ps,lin})$ . This follows the linear model for deep water swells at great distances from their generation areas, as given by *Barber and Ursell* [1948]. In this model the swell energy travels along the great circle of direction  $\theta_{ps}$  at the observation point, with a group speed, prescribed by deep water linear wave theory, namely  $C_g(f) = g/(4\pi f)$ . The space-time correspondence of  $f_{ps,lin}$  and  $\theta_{ps,lin}$  are given by

$$f_{ps,lin} = \frac{g(t - t_s)}{4\pi R\alpha}, \quad (1)$$

$$\theta_{ps,lin} = \arccos\left(\frac{\sin \phi_s - \sin \phi \cos \alpha}{\sin \phi \sin \alpha}\right), \quad (2)$$

and

$$\alpha = \arccos(\cos \phi \cos \phi_s \cos(\lambda - \lambda_s) + \sin \phi \sin \phi_s), \quad (3)$$

where  $\alpha$  is the angular distance between the point source of coordinates  $(\lambda_s, \phi_s)$  and the observation point of coordinates  $(\lambda, \phi)$ ,  $t_s$  denotes the time of the source event and  $t$  the observation time,  $R$  denotes the Earth radius and  $g$  the acceleration of gravity. The linear time dependence of  $f_{ps,lin}$  at a given point is consistent with the ridge-like pattern in the time-frequency diagrams of the wave energy, conspicuous in any measurement of remote swells [e.g., *Munk et al.*, 1963]. The investigations of *Snodgrass et al.* [1966] and *Hasselmann et al.* [1996], among others, confirmed the ability of the model (1)–(3) to estimate the space-time structure of directions and frequencies when cutting across a swell field along a great circle.

[17] We decide that a partition belongs to a swell field if and only if the relative spectral distance between observed and expected values of  $(f_{ps}, \theta_{ps})$

$$D(f_{ps}, \theta_{ps}) = \frac{1}{f_{ps}} \left[ (f_{ps} \cos \theta_{ps} - f_{ps,lin} \cos \theta_{ps,lin})^2 + (f_{ps} \sin \theta_{ps} - f_{ps,lin} \sin \theta_{ps,lin})^2 \right]^{\frac{1}{2}} \quad (4)$$

is below a fixed threshold of 0.3. This threshold has been calibrated to be relatively strict, as we would rather be sure

that only contributions to the field of interest are retained rather than trying to keep more contributions which present stronger differences with deep linear propagation from a point source. As a result, this criterion is almost never met close to the source, and the fields obtained usually have gaps near the source. Since the present work is mostly concerned with medium to far fields from the source, this is not important. Filling the hole near the source could be done by relaxing the constraint on  $D$  and using the continuity of  $f_{ps}$  and  $\theta_{ps}$  fields, as done by, e.g., *Gerling* [1992] or *Hanson and Phillips* [2001].

[18] At a given point the partition which minimizes the distance  $D$  is further selected, so that at any location only a single partition is part of the field. This requires that the input spectra are smooth enough so that noise is not mistaken for multiple peaks [e.g., *Portilla et al.*, 2009].

[19] The present work uses model spectra that are smooth enough and SAR data that is smoothed before partitioning. When using buoy data, the time average and the interpolation of the spectra on the model frequency grid make the spectra smooth enough for a simple partitioning (see section 2 for data description). In order to be consistent with the propagation model (1)–(3), only long swells with peak frequency lower than 0.08 Hz are considered below.

### 3.2. Structure of Swell Fields

[20] Two examples of swell fields are presented. The storms investigated in this paper are part of the database further analyzed by *Ardhuin et al.* [2009a] for which the storm location was also verified against Quikscat satellite wind fields obtained from CERSAT.

[21] In Figure 1, the tracking method is applied to partitioned spectra derived from the NDBC platforms 51028 and 46029. The tracked swell system has been generated by a storm which occurred in the southwest Pacific Ocean on 9 July 2004 and was centered at 177°E, 55°S. This particular 9 July 2004 storm is also illustrated by Figures 2 and 3 of *Collard et al.* [2009]. Swell parameters are compared with the tracking result obtained from the spectra computed by WWATCH.

[22] As often reported, the peak frequency and direction time series are in excellent agreement with the model given by (1)–(3) and thus with the numerical model WWATCH, which is based on the same geometrical optics principle, with limited numerical error [*Wingert et al.*, 2001; *Tolman*, 2002]. The peak direction  $\theta_{ps}$  varies weakly around the source direction 200° for 51028 and 220° for 46029. The normalized root mean square difference (NRMSD) between the WWATCH model and the observations is of 3.9% and 2.8%, respectively, for these two time series, where the NRMSD between time series of model results  $(X(t_i))_{i=1..n}$  and observations  $(Y(t_i))_{i=1..n}$  is defined by

$$NRMSD = \frac{1}{RMS} \left( \frac{1}{n} \sum_{i=1}^n (X(t_i) - Y(t_i))^2 \right)^{\frac{1}{2}}, \quad (5)$$

with  $RMS$  the root mean square of  $(Y(t_i))_{i=1..n}$ . It has been further verified on other storms (not shown) that the observed peak periods and those obtained with the numerical wave model coincide very closely. Compared to both

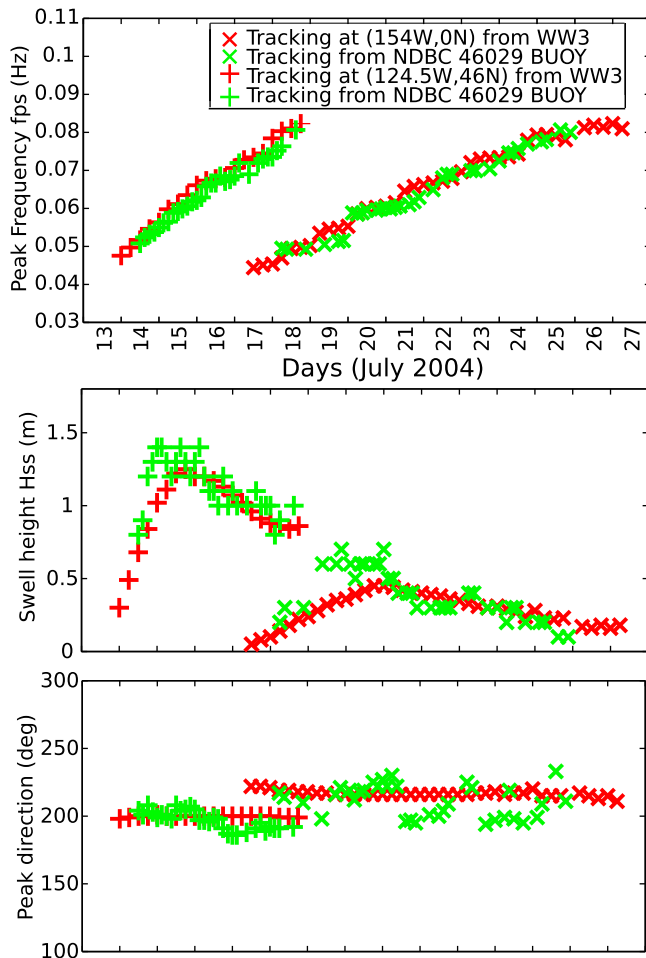


**Figure 1.** Parameters of a swell field, generated by a storm centered at  $177^{\circ}\text{W}$ ,  $55^{\circ}\text{S}$  on 9 July 2004. Results are shown with green plus signs for NDBC buoy data 51028 (central equatorial Pacific) and green crosses for 46029 (off the Oregon-Washington border). Model results for the same locations are processed in the same way and shown with red symbols.

observations and model results, the point source model gives arrival times that are on average 6 h too early for 17 s swells and up to 18 h too early for 13 s swells, with a gradual increase for intermediate periods, for all propagation distances. This effect will not be corrected in the following processing. It suggests that the afterglow of the storm, when the winds are decreasing, may be the time where most energy is generated for the shorter swells. That property could be used to refine the point source model.

[23] Swell dispersion also induces a progressive separation of the lowest- and highest-frequency components, resulting in larger durations of the swell events as the distance from the source increases. Here the swell is significant for 5 days at buoy 51028, located 6800 km from the source, and 9 days at 46029, located 10,900 km from the source (see Figure 1).

[24] The modeled  $H_{ss}$  are clearly less accurate than frequencies or directions, with NRMSDs of 14.1% and 27.5% at 51028 and 46029, respectively. These high NRMSD values are typical of such long swells whereas significant

wave height of the total sea state  $H_s$  is generally better predicted by this state-of-the-art model, in the range 5–15% for the open ocean, in particular on the eastern part of ocean basins [Ardhuin *et al.*, 2009b, 2010].

[25] From these comparisons of model and buoy observations it appears that periods and directions are well described by equations (1)–(3), but there is a need to improve the predictions of  $H_{ss}$ , which requires a further understanding of the structure of the  $H_{ss}$  field and possibly the assimilation of observations based on such structures.

[26] However, qualitative features of the time series seem to be well reproduced by the model: a rapid increase of  $H_{ss}$  precedes an energetic peak with frequencies close to 0.06 Hz (periods close to 17 s) and directions around  $200^{\circ}$  for 51028 and  $220^{\circ}$  for 46029, followed by a slower decrease of  $H_{ss}$  with the gradual arrival of higher-frequency components of the system.

[27] Figures 2 and 3 illustrate the application of the swell systems tracking method to the model. Figure 2 represents the peak period ( $T_{ps}$ ) and significant wave height fields on 3 June 2004 at 0000 UTC for the 3 most energetic partitions obtained by partitioning WWATCH spectra. In Figure 2, the parameters  $H_{ss}$  and  $T_{ps}$  are shown for partitions with decreasing energy. From one point to the next of the ocean surface, this local ordering can make the swell system jump from one storm source to another. As a consequence, the structure of the crossing swell fields from separate sources is difficult to understand from the peak periods (Figure 2, left). The significant wave height field by itself is even more difficult to interpret.

[28] Figure 3 represents the results of the tracking method applied to the same partitions. The tracked swell system has been generated by a source event which occurred in the northwest Pacific Ocean on 24 February 2004 and was centered at  $160^{\circ}\text{E}$ ,  $42^{\circ}\text{N}$ . Results are given at 3 day intervals on 27 February, 1 March 2004, and 6 March 2004, all at 0000 UTC. The tracking algorithm provides a selection of the particular swell field related to the chosen source, among the many crossing swell fields that emanate from other sources (seen in Figure 2). A remarkable coherence of the peak period field is now observed. This coherence seems to be very little affected during the propagation and is still observed at very long distance from the source (on Figure 3f, the system is located at more than 9000 km from its source). The peak period field exhibits a conservation of a structure that is in good agreement with the model (1)–(3). The dispersion-induced spreading in the propagation direction is also clearly visible from Figure 3a to Figure 3c.

[29] The structure of the  $H_{ss}$  field appears more complex. On Figure 3a, the distribution of  $H_{ss}$  for different outgoing directions results from the wave generation in the storm. Farther from the source, a general decrease of  $H_{ss}$  with the distance from the source is observed. Outside of the areas sheltered by islands, this decrease of  $H_{ss}$  is mainly due to dispersion and angular spreading, with a secondary effect of dissipation [Collard *et al.*, 2009; Ardhuin *et al.*, 2009a].

[30] We will now further analyze the space-time structure of the  $H_{ss}$  field of long-swell systems. Because the model results provide a continuous coverage in space and time, the modeled  $H_{ss}$  fields are first analyzed. The fair qualitative agreement of model predictions with observations suggests

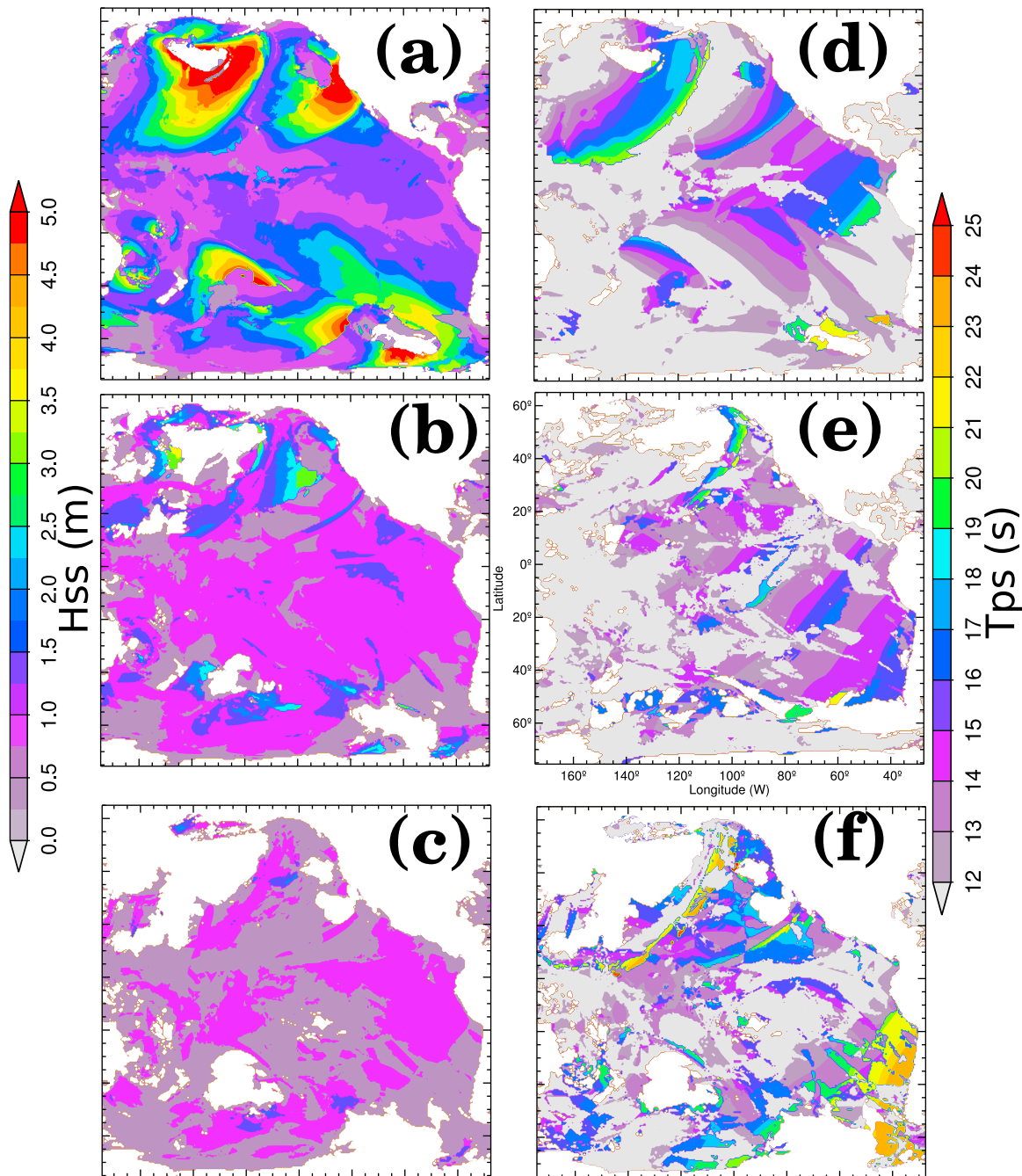


**Figure 2.** (left) Modeled peak periods and (right) significant swell heights for the three most energetic swell partitions on 3 June 2004, at 0000 UTC. The locally (a and d) first, (b and e) second, and (c and f) third partition by decreasing order of energy are shown. In black are the areas where no swell partition is detected.

that some features found here are probably also present in the observations, which will be verified in section 5.

#### 4. Patterns of Modeled Swell Heights

##### 4.1. Significant Wave Heights Correlations

[31] The spatial structures of the total  $H_s$  fields, and not  $H_{ss}$  as studied here, have been investigated by e.g., *Greenslade and Young* [2005]. These structures were studied in the context of sequential assimilation systems and the time

correlation has been given relatively less attention [*Pinto et al.*, 2005]. Yet, in the very early swell investigations, correlations of swell height time series have been examined. When confronted with the task of practically improving the swell forecasting method of *Gain* [1918], based on the analysis of storm paths in the North Atlantic, *Montagne* [1922] soon realized that swell heights observed in the Azores corresponded closely, for many storms, with the observations of his own services in Morocco, with a time shift due to the time of propagation. Similar conclusions

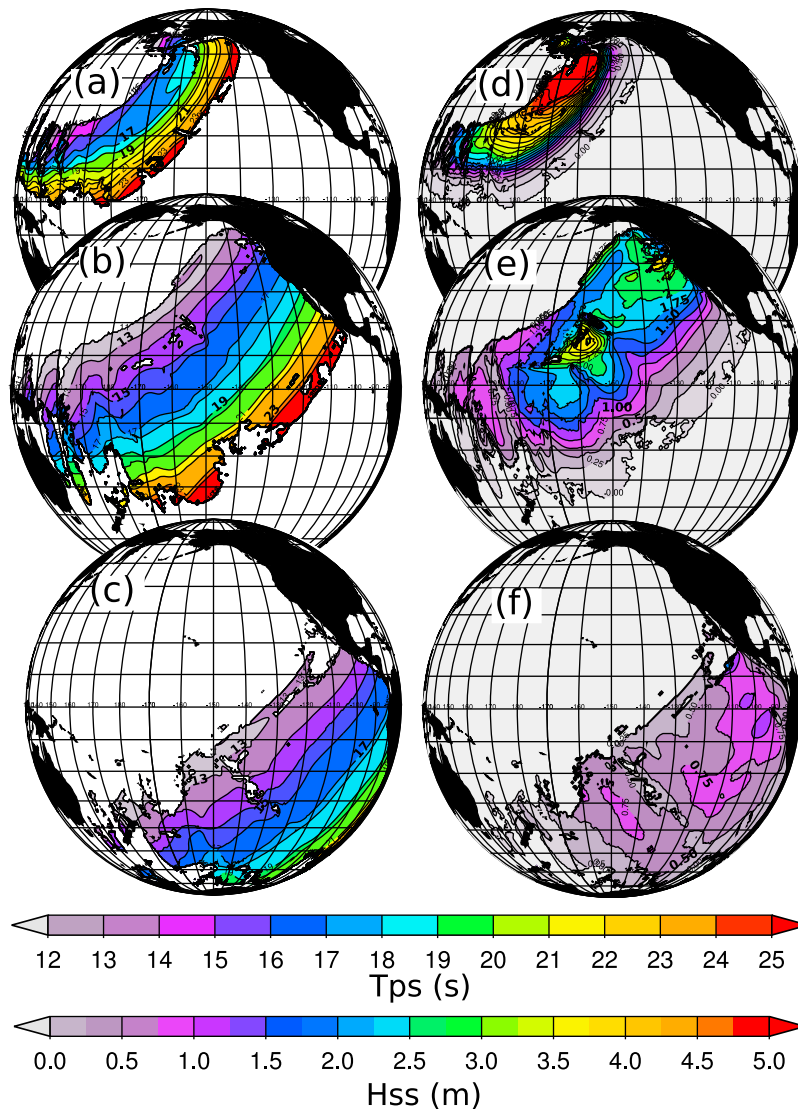


**Figure 3.** Space-time tracking of a modeled swell system illustrated by (left) the peak periods  $T_{ps}$  and (right) the swell heights  $H_{ss}$ . The tracked system has been generated by the storm which occurred on 24 February 2004 at  $160^{\circ}\text{E}$ ,  $42^{\circ}\text{N}$ . The system is shown on (a and d) 27 February, (b and e) 1 March, and (c and f) 6 March at 0000 UTC. The central longitude is  $150^{\circ}\text{W}$ . The crossing swells present at that time have been filtered out by the tracking procedure.

were also drawn on the relation of microseismic activity in Europe compared to swells in Morocco [Bernard, 1937].

[32] Following these observations, we shall thus investigate correlations between  $H_{ss}$  time series of a given swell system at two different points. These correlations are obviously expected to change from event to event, with possibly some common features. After choosing a reference point  $P_0$ , the correlation between the time series at  $P_0$ ,  $H_{ss,0}(t_i)$  for  $i$  in  $\{1..n\}$ , and at any other point  $P_j$ ,  $H_{ss,j}(t_i)$ , is investigated.

[33] Pearson's linear correlation coefficient  $C_j$  is used, allowing for a time shift  $\tau_j$ , so that  $C_j$  is given by

$$C_j = \frac{\sum_{i=1}^n (H_{ss,0}(t_i - \tau_j) - \overline{H_{ss,0}})(H_{ss,j}(t_i) - \overline{H_{ss,j}})}{(n-1)\sigma_0\sigma_j}, \quad (6)$$

where  $\overline{H_{ss,0}}$  and  $\sigma_0$  are given by

$$\overline{H_{ss,0}} = \frac{1}{n} \sum_{i=1}^n H_{ss,0}(t_i) \quad (7)$$

and

$$\sigma_0 = \left( \frac{1}{n-1} \sum_{i=1}^n (H_{ss,0}(t_i) - \overline{H_{ss,0}})^2 \right)^{\frac{1}{2}}, \quad (8)$$

with similar definitions for  $\overline{H_{ss,j}}$  and  $\sigma_j$ .

[34] Figure 4 represents the result without time shift ( $\tau_j = 0$ ) obtained for the system generated by the source event which occurred on 16 February 2004 at 0000 UTC and was cen-

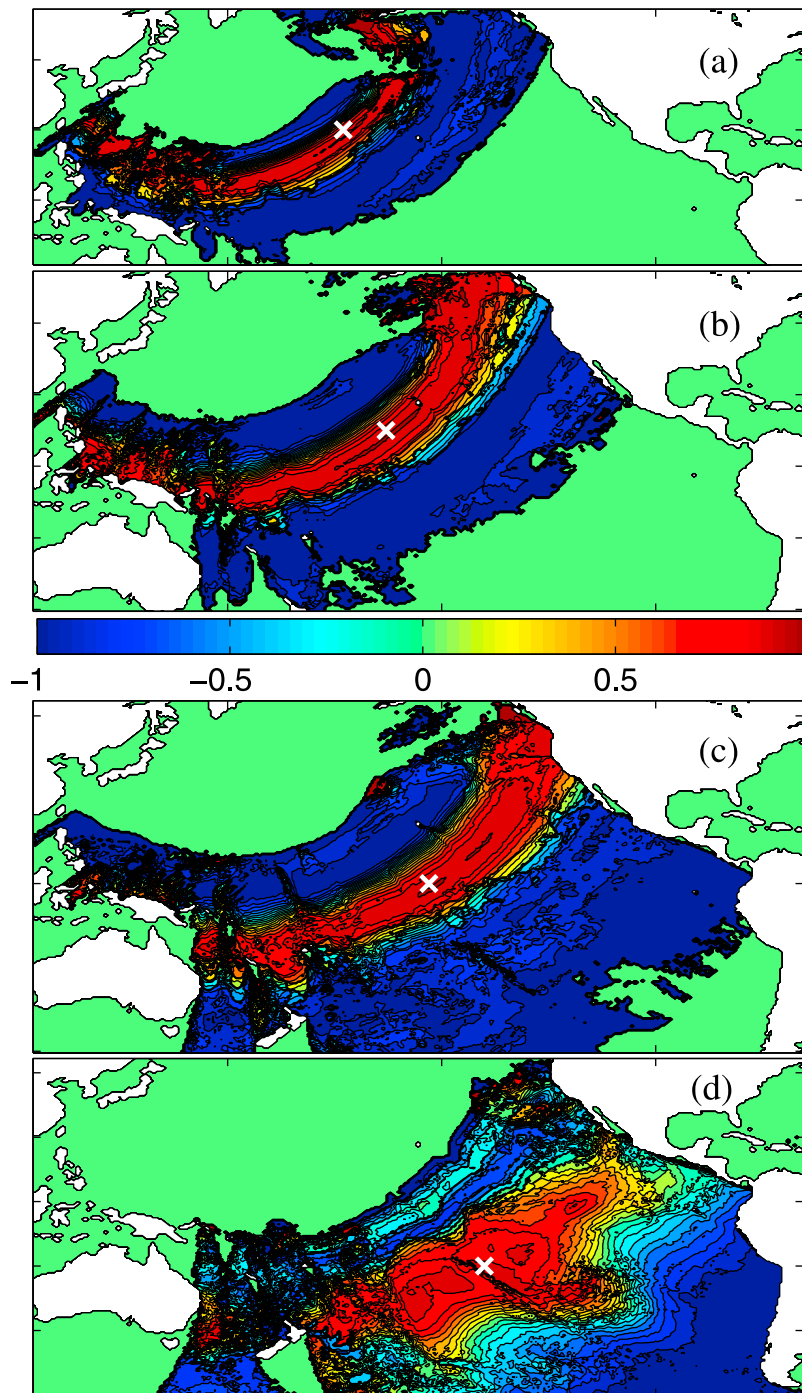


**Figure 4.** Significant wave height time series correlations between a reference point  $P_0$  (white cross) and the other points for the source event occurring on 16 February at 0000 UTC: (a)  $P_0 = (173^\circ\text{W}, 20^\circ\text{N})$ , (b)  $P_0 = (163^\circ\text{W}, 10^\circ\text{N})$ , (c)  $P_0 = (153^\circ\text{W}, 0^\circ\text{N})$ , and (d)  $P_0 = (130^\circ\text{W}, 20^\circ\text{S})$ .

tered at  $160^\circ\text{E}, 37^\circ\text{N}$ . The value of  $C_j$  for this swell system is given at  $P_j$  by the color scale, if the system is simultaneously detected in  $P_0$  and  $P_j$  during at least 24h. Figures 4a–4d correspond to  $P_0=(173^\circ\text{W}, 20^\circ\text{N})$ ,  $P_0=(163^\circ\text{W}, 10^\circ\text{N})$ ,  $P_0=(153^\circ\text{W}, 0^\circ\text{N})$ , and  $P_0=(130^\circ\text{W}, 20^\circ\text{S})$ , respectively. On Figures 4a–4d, the location of  $P_0$  is represented by a white cross.

[35] These results show a remarkable  $H_{ss}$  correlations structure. On Figures 4a–4c, strong correlations ( $C_j > 0.9$ ) are observed for all the points located on the arc of a circle, at the same distance from the source as  $P_0$ . These strong correlations are observed for all the propagation directions. This is not too surprising since the basic time series of rising and falling  $H_{ss}$  is likely to be a common feature of any

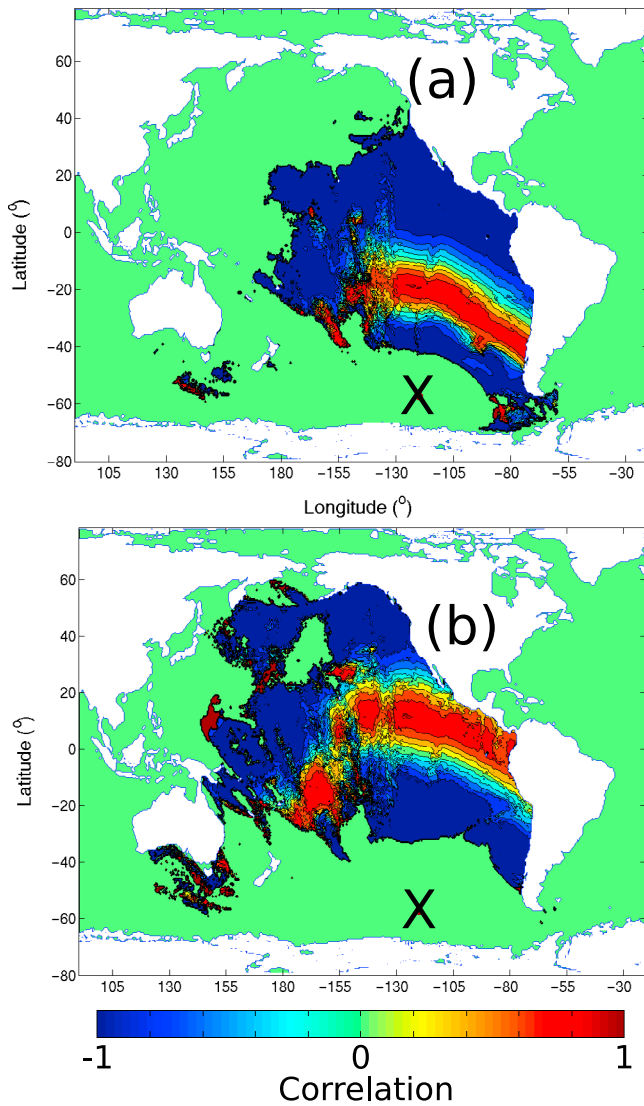


**Figure 5.** Same as Figure 4 but for the 9 August 2004 storm, with  $P_0$  at (a)  $124^\circ\text{W}, 17^\circ\text{S}$  or (b)  $125^\circ\text{W}, 12^\circ\text{N}$ , correlated with times series at other locations. The black cross indicates the source location.

localized source, but the high correlation level indicates a degree of similarity that may be used to reconstruct a field from sparse data, even for locations not aligned with other observations. These remarkable features are observed for all the different swell systems studied here. Whereas Figure 4 shows a rather isotropic correlation structure, the correlation pattern for the swell shown in Figure 5 appears less isotropic, probably due to the translation speed and rotation of the generating storm. The area of high correlation at  $10^\circ\text{S}$  and  $160^\circ\text{W}$  is located at a distance closer to the source than the east part of the high correlations front, probably because the associated waves were generated at different stages of the storm evolution.

[36] However, for all the systems, the area with strong correlations is less regular and symmetric at very long distance from the source (more than 7000 km on Figure 4d). The principal cause of this evolution appears to be island shadowing. Indeed, the most important changes in correla-

tion are located in the shadow areas of Pacific islands. In the examples presented in Figure 4, the decrease in correlation is mostly to be found in the south west region of the Pacific basin, where the swell field propagated between many islands. Obviously the stretching of the time series due to dispersion (Figure 1) is another source of decorrelation that could be easily corrected for, but we preferred to keep the simplest form possible.

#### 4.2. Structure of Swell Height Fields in the Transverse Direction

[37] The strong correlations observed in the direction orthogonal to the propagation direction suggest that the ratio between the swell system  $H_{ss}$  simultaneously observed at two points is nearly time independent and thus frequency independent given equation (1), if the two points are located at the same distance from the source.

[38] This leads to define a coefficient  $r(\alpha, \beta)$  that is representative of this  $H_{ss}$  ratio, where  $\alpha$  and  $\beta$  are the colatitude and longitude when setting the North Pole on the storm center. Here we chose to examine the averaged ratio between the system energy simultaneously observed at two points located at the same distance from the source, where the average is taken over the different frequency components of the system. We shall use this definition for  $r$

$$r(\alpha, \beta) = \sqrt{\frac{1}{n} \sum_{i=1}^n \frac{H_{ss}(\alpha, \beta, t_i)^2}{H_{ss}(\alpha, \beta_r, t_i)^2}}, \quad (9)$$

where  $\beta_r$  is a fixed reference direction. Figures 6a and 6b give two representations of  $r$  for the system generated on 16 February 2004 at  $160^\circ\text{E}, 37^\circ\text{N}$  for distances  $\alpha$  from  $30^\circ$  to  $100^\circ$ , with a  $10^\circ$  step. Defining  $\beta_r$  as the closest direction from the system mean direction outside the source in which waves do not cross island groups,  $\beta - \beta_r$  takes values in the range  $[-180^\circ, 180^\circ]$  and we compute  $r(\alpha, \beta)$  every  $8^\circ$ .

[39] Figure 6a gives the location of the points where the ratio  $r$  is computed, with the value of  $r$  indicated by the color scale. Figure 6b gives transverse profiles of  $r(\alpha, \beta)$  for the different values of  $\alpha$  and this time the color scale indicates the value of  $\alpha$ .

[40] Figure 6b reveals that the transverse structure is essentially the same for different values of  $\alpha$ , except for islands shadow regions. For example the shadow of the Tuamotus (French Polynesia,  $20^\circ\text{S}, 140^\circ\text{W}$ ) explains the change of  $r$  for  $\beta = \beta_r + 40^\circ$  as  $\alpha$  increases from  $60^\circ$  to  $70^\circ$ .

[41] The variability imposed by islands appears to be significant for large islands groups, such as the Hawaii chain ( $20^\circ\text{N}, 155^\circ\text{W}$ ) for  $\alpha > 40^\circ$  and  $\beta - \beta_r \sim 10^\circ$  or the Tuamotus. Outside of these main island shadow zones,  $r(\alpha, \beta)$  generally varies very little with  $\alpha$ . This low variability is a common feature of all the different systems studied here (see Figures 7 and 8 for other examples).

#### 5. Estimation of Transverse Structures in SAR Data

[42] The structure of the modeled  $H_{ss}$  fields is now verified. Because we expect a similar smooth variation of  $H_{ss}$  with  $\alpha$ , we build an estimate of  $r(\alpha, \beta)$  using SAR data. We define the structure function  $r(\alpha_0, \beta)$  by propagating SAR

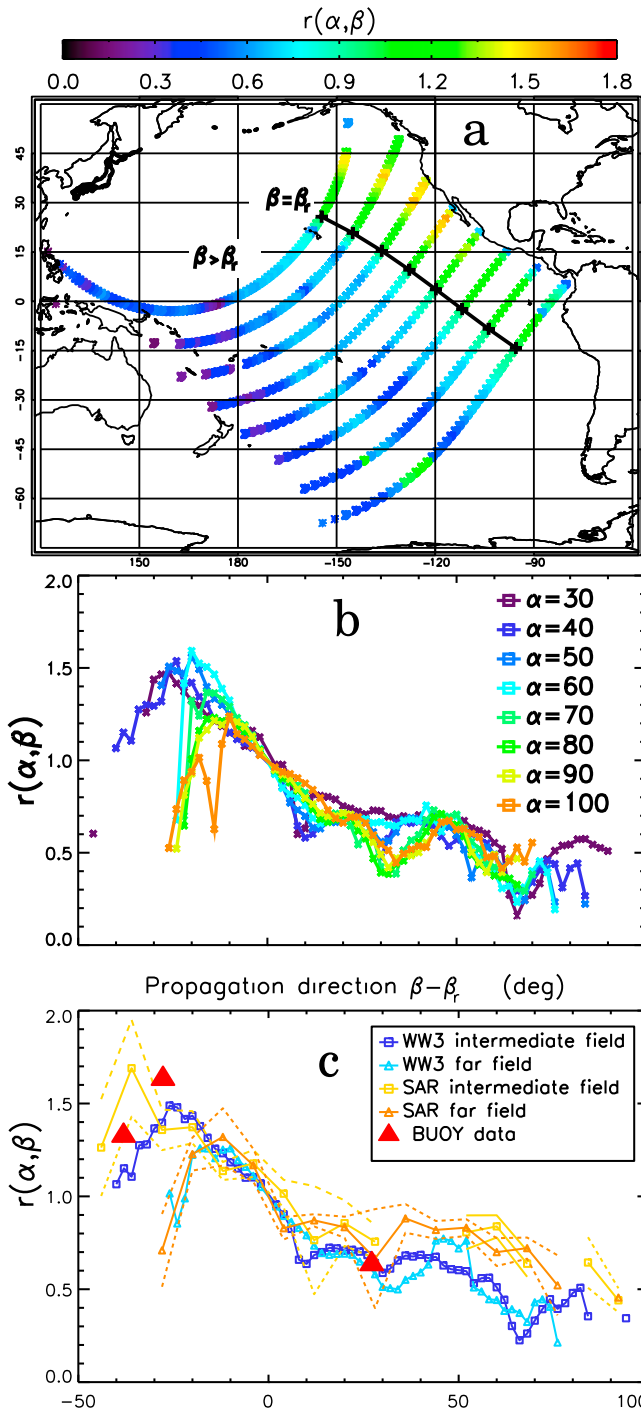


**Figure 6.** Transverse structure of the system generated on 16 February 2004, at 160°E, 37°N. (a) Spatial distribution of  $r(\alpha, \beta)$ , inferred from the model, with the reference direction  $\beta_r$ , in black. (b) Transverse profiles of  $r(\alpha, \beta - \beta_r)$  for the model only. (c) Transverse profiles of  $r(\alpha, \beta - \beta_r)$  for intermediate ( $\alpha < 60^\circ$ ) and far fields ( $\alpha > 60^\circ$ ) inferred from model, SAR, and buoy data. The dashed lines correspond to  $\pm 1$  standard deviation of the expected SAR error given the scatter index of SAR observations compared to buoys [Collard et al., 2009], divided by  $\sqrt{N}$  where  $N$  is the number of SAR observations for one given estimate of  $r$ .

observations located at distances  $\alpha$  in the range  $[\alpha_1, \alpha_2]$  to the distance  $\alpha_0$ . This propagation is similar to the generation of “fireworks” described by Collard et al. [2009], but the value of  $H_{ss}(\alpha, \beta)$  given by the SAR observation is now rescaled by a factor of

$$\frac{r(\alpha_0)}{r(\alpha)} = \sqrt{\frac{\alpha \sin \alpha}{\alpha_0 \sin \alpha_0}}, \quad (10)$$

which corresponds to a propagation without dissipation away from a point source [e.g., Collard et al., 2009].

[43] Because of the limited number of SAR observations, the resolution is limited over  $\alpha$  or  $\beta$ . Since we wish to examine details in the  $\beta$  dimension, a very coarse resolution in the  $\alpha$  dimension is taken by dividing up the oceans in an intermediate field, with  $40^\circ \leq \alpha \leq 60^\circ$  and a far field with  $\alpha > 60^\circ$ . Observations for  $\alpha < 40^\circ$  are not retained because equation (10) is not generally valid in the near field.

[44] Figure 6c represents the result obtained for the 16 February 2004 (160°E, 37°N) storm. On Figure 6c, the intermediate field and far field structures estimated from the model are also superimposed.

[45] A good agreement of the different structures appears in the east part of the Pacific basin, for  $\beta - \beta_r < 0^\circ$ , where few islands are in the propagation path. On the contrary, for

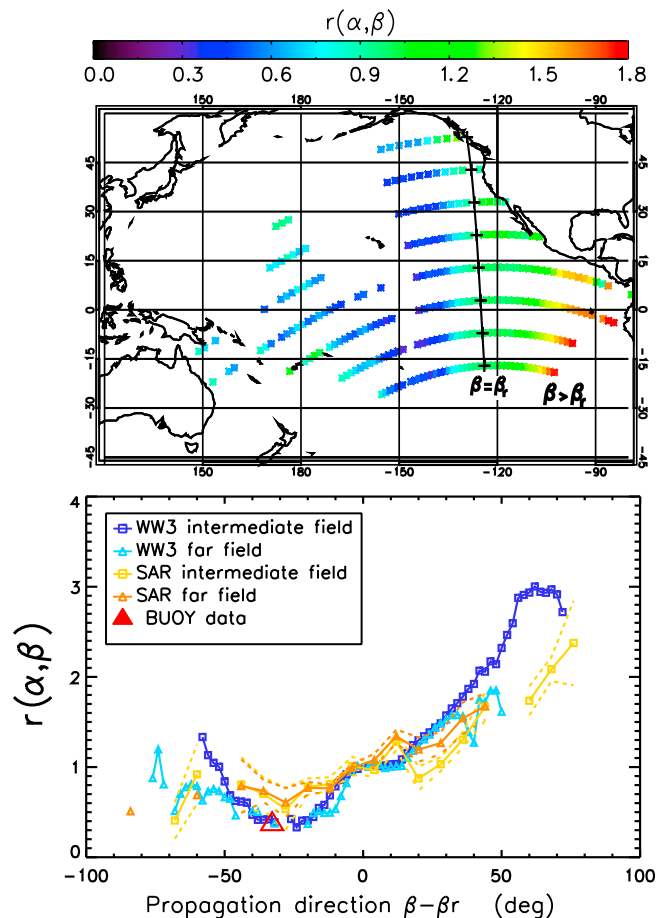


**Figure 7.** Same as Figure 6 but for the storm which occurred on 9 August 2004 at 0000 UTC, located at 120°W, 57°S.

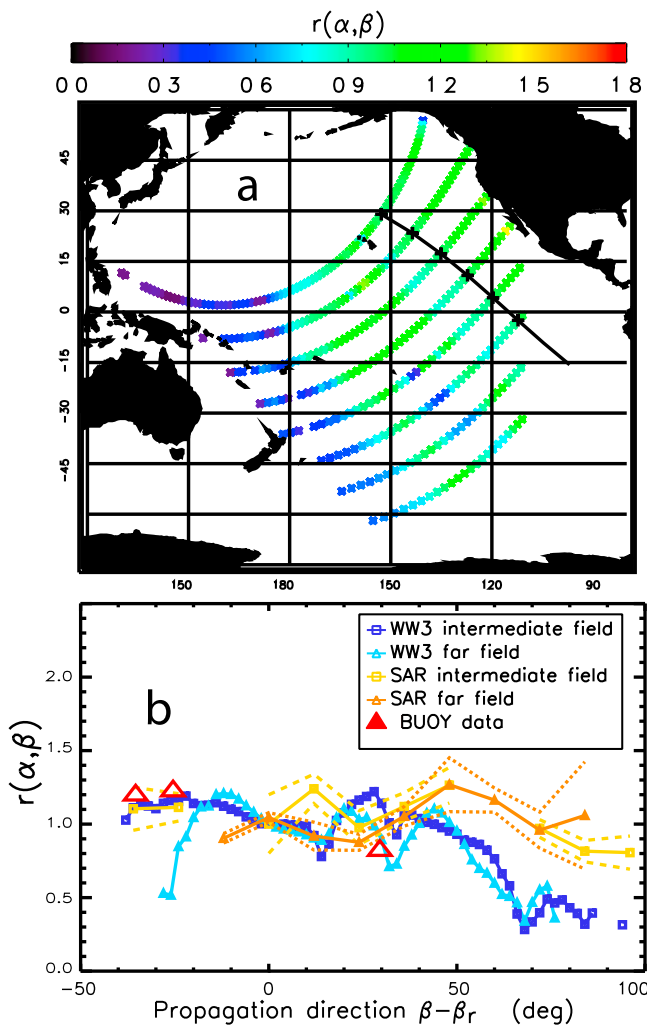


**Figure 8.** Same as Figure 6 but for the 24 February 2004 storm.

$\beta - \beta_r > 0^\circ$ , modeled  $H_{ss}$  are underestimated. This low bias also exists in the close field structure. Outside of island shadows, the model and SAR observations generally show little variability (Figures 5–8) with some exceptions. Figure 8 shows that the model particularly underestimates the swell field energy for  $\beta - \beta_r > 50^\circ$ . This is probably due to an initial bias introduced during the swell generation, possibly an error in the forcing winds or in the forcing function of the model.

[46] For a given value of  $\alpha$ ,  $r$  generally exhibits a peak with a very slow decrease with  $\beta$ . The half width of  $r$  is typically larger than  $60^\circ$ . In the case of the 24 February 2004 storm,  $r$  is almost isotropic with  $\beta$ . Model results appear less isotropic than SAR observations, possibly due to an incorrect dependence of the swell damping rate on the wind-wave angle in the parameterization by *Ardhuin et al.* [2009b], or similar defects in the forcing wind fields or wind-wave generation parameterization.

[47] Analysis of modeled spectra thus suggests a large-scale coherence of the space-time  $H_{ss}$  field structure, with

a transverse structure imprinted by the source storm and islands shadows.

## 6. Modeling $H_s$ Structure of a Swell System: Synthetic Field

[48] Given the features of the  $H_{ss}$  field, there may be a use for parameterized synthetic fields that could represent the correlations of  $H_{ss}$ , for example in an assimilation system for wave hindcasting or forecasting. For simplicity we propose such a parameterization of  $H_{ss}$  outside island shadows.

[49] Given the generally good approximation of  $T_{ps}$  and  $\theta_{ps}$  with  $T_{ps,lin}$  and  $\theta_{ps,lin}$ , periods and directions space-time structures are represented by the deep water linear propagation from a point source (1) and (2). The temporal shift  $\tau$  which maximizes the correlation of  $H_{ss}$  time series observed at two points  $P_0$  and  $P$  located at distances  $\alpha_0$  and  $\alpha$ , respectively, from the storm is replaced by

$$\tau(\alpha, t) = \frac{4\pi R(\alpha - \alpha_0)f_{ps,lin}}{g}, \quad (11)$$

where  $f_{ps,lin}$  is given by (1) at the point  $P$  at time  $t$ .

[50] Secondly, we seek a parameterization for  $r$  by separating the variables, with a form  $r(\alpha, \beta) = r_1(\alpha)r_2(\beta)$ . It is further assumed that  $r_1$  is given only by the principal causes of  $H_{ss}$  decrease, namely dispersion and angular spreading, which is represented by the asymptotic form (10).

[51] This gives the parameterized field

$$\hat{H}_{ss}(\alpha, \beta, t) = \sqrt{\frac{\alpha_0 \sin \alpha_0}{\alpha \sin \alpha}} H_{ss,0}(t - \tau(\alpha, t)) r(\beta), \quad (12)$$

where  $H_{ss,0}(t)$  is a known reference  $H_{ss}$  time series at the point  $(\alpha_0, \beta_0)$ , given by an in situ sensor or inferred from a broadband seismograph [e.g., *Bromirski et al.*, 1999].

[52] The field (12) is now compared to observations. Using the storm of 16 February 2004 as an example, we use for  $H_{ss,0}(t)$  the  $H_{ss}$  time series given by the Christmas Island buoy (number 51028). Here  $\tau$  is defined using equation (11) in which  $f_{ps,lin}$  is replaced by the time-dependent peak period time series at the buoy. This very simple approximation could be refined by taking the spectral content given by the buoy. We use for  $r_2(\beta)$  the intermediate field structure estimated from SAR observations and thus reconstruct a synthetic field  $\hat{H}_{ss}$  using (12), which is compared with SAR observations in the far field.

[53] Figures 9a and 9b represent the synthetic  $\hat{H}_{ss}$  field obtained at two different times: on 25 February 2004, when it is mostly in the intermediate field, and on 28 February 2004, when it is mostly in the far field, both at 0000 UTC.

[54] Figures 9c and 9d represent the modeled field extracted from the model computation at the same times. Figure 10 represents the relative error between  $\hat{H}_{ss}$  and SAR observations (Figures 9a and 9c) and between modeled  $H_{ss}$  and SAR observations (Figures 9b and 9d) in the far field region. As the synthetic  $\hat{H}_{ss}$  field represents the  $H_{ss}$  field outside islands shadow, only SAR observations which are located outside this shadow are considered here. In practice, an observation is not retained if the great circle

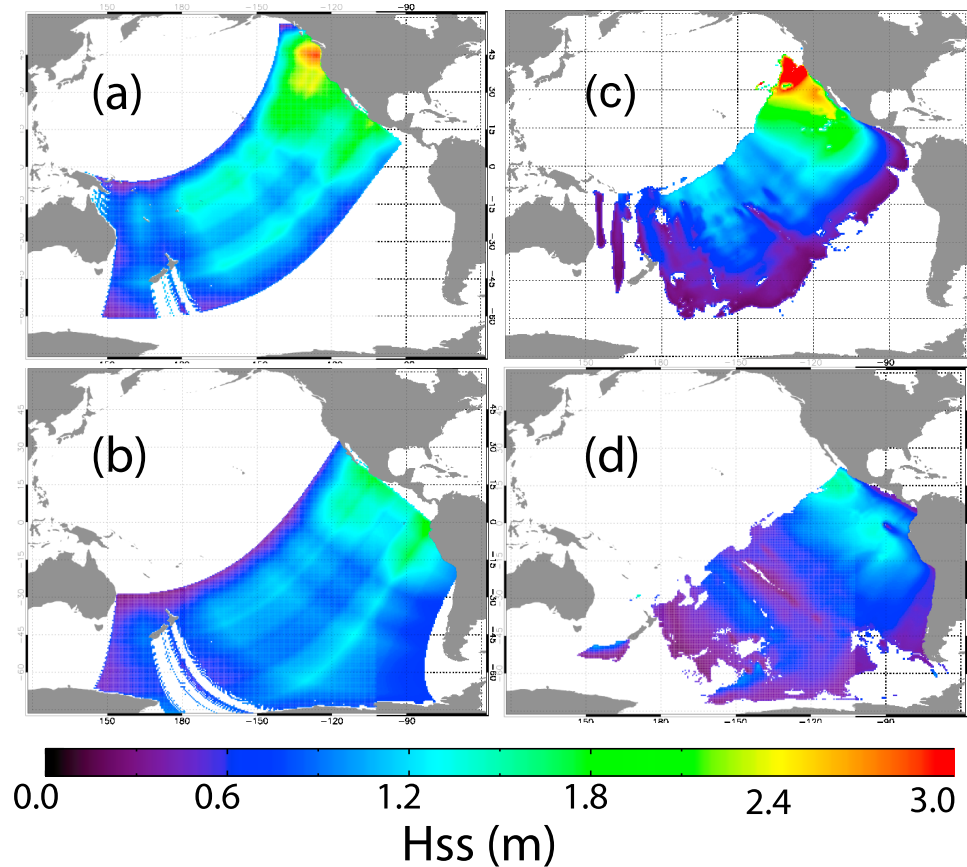


**Figure 9.** (a and c) Synthetic field of  $H_{ss}$  on 25 and 28 February 2004. (b and d) Modeled field at the same time.

path joining its location to the source point is less than 20 km from an important island.

[55] Clearly the synthetic swell field is very smooth due to the many simplifying assumptions, in particular for the decay along the propagation path. Yet, the modeled and synthetic fields present a global NRMSD of 35.4% and 33.6%, respectively, suggesting that our very crude first parameterization does capture the essential features of the swell field, up to a point that it may already be useful as a correction for today's best numerical models.

[56] Although the variation of  $H_{ss}$  with  $\alpha$  in Figure 9 does not look very realistic, the key element here is certainly the variation of  $H_{ss}$  with  $\beta$ . Indeed, as mentioned in section 5, the model notably underestimates the swell field energy in this part of the basin (Figure 8 for  $\beta - \beta_p > 50^\circ$ , in particular to the East of New Zealand). Such a model underestimation is likely due, in part, to an exaggerated island blocking in the model, consistent with the general low bias of the model in French Polynesia [Ardhuin *et al.*, 2010]. Although the global performance may not sound impressive, the synthetic field has errors lower by a factor of 2 in this region, and could thus be used to correct model predictions.

[57] The lower NRMSD for the systems components whose propagation path crosses few islands confirms the good agreement of (12) with the observations. It should be noted that these differences are not much larger than the expected error of SAR-derived  $H_{ss}$  which is about 24%. It is thus likely that the benefits are larger than suggested by

comparison with individual SAR observations. A further quantitative validation should be performed with (more accurate) buoy measurements, or by aggregating SAR observations over a finite time frame and spatial extent.

## 7. Conclusions and Perspectives

[58] Several studies from Montagne [1922] and Barber and Ursell [1948] to Collard *et al.* [2009] have shown that long-swell systems often follow closely wave linear theory for a point source, and swells may travel with high space-time correlations over distances and times as large as 10,000 km and 10 days. However, because the variations of swell wave height  $H_{ss}$  were not known as a function of the direction  $\beta$  transversal to the propagation, previous investigations of swells for forecasting or geophysical applications had to rely on measurements aligned along propagation great circles [e.g., Snodgrass *et al.*, 1966]. Here we have performed the first investigation of  $H_{ss}$  as a function of  $\beta$ . Although the analysis of many more swell events will be needed to accumulate confidence in these results, two important results are obtained.

[59] First, the distribution of  $H_{ss}$  is very broad, broader than  $\cos \beta$ , so that a swell field generally covers a very large part of an ocean basin, with some occasional propagation into other basins [Alves, 2006]. As a result, the correlations of geophysical processes with swell can be very difficult to interpret, and nonlocal swell effects may be mistaken as

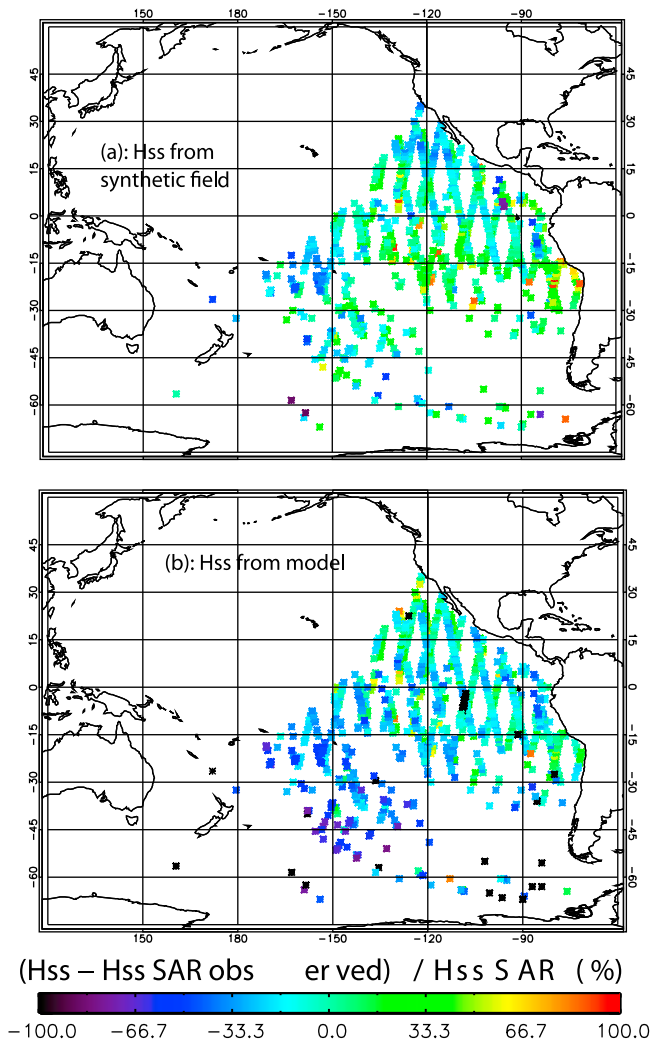


**Figure 10.** Normalized difference  $(H_{ss} - H_{ss,SAR})/H_{ss,SAR}$  for  $\alpha > 60^\circ$ , for (a) the synthetic wave field and (b) the model results.  $H_{ss,SAR}$  is derived from the local SAR observations.

local effects. For example, while both midocean and coastal sources of microseisms coexist, it is hard to distinguish microseismic signals generated at a coast [e.g., Bromirski *et al.*, 1999] from other microseismic signals generated in deep water [e.g., Kedar *et al.*, 2008].

[60] Second, the variations of  $H_{ss}$  are largely invariant as a function of distance from the storm  $\alpha$ , except for island shadow effects. As a result, the swell field can be parameterized by separating the variables  $\beta$  and  $\alpha$ , with the time closely related to  $\alpha$  due to the propagation. In one example, a first crude parameterization of  $H_{ss}$  based on this principle was shown to agree already slightly better than the best forecasting model available today [Bidlot, 2008]. There is thus a clear potential for improving swell hindcasts and forecasts by developing time-dependent covariance models based on these observations, or by directly assimilated gridded (level 3) synthetic swell parameters. Clearly, the parameterization of islands in the synthetic swell fields is an obvious next step, and this could easily use the subgrid masking algorithms employed in wave models [Tolman, 2003]. This was not done here in order to keep the proce-

cedure as simple as possible and also because no detailed local validation of these algorithm has yet been performed. The simple decay law for  $H_{ss}$  with distance  $\alpha$  could also be refined to represent explicitly the spectral contents of the wave field and include a period-dependent dissipation rate, based on, e.g., Ardhuin *et al.* [2009a]. Further methodological improvements may come from a comprehensive study of swell fields, that may show how and when  $H_{ss}$  may be directly parameterized based on the storm structure, translation and rotation. It is quite possible that our procedure for assembling swell fields has biased our view of swells toward fields that do conform well to the point source model, and we will further examine how representative these fields are.

[61] The validation of the features first presented in this paper, and the further investigations suggested above are planned to benefit from the data collected by the future China-France Ocean Satellite (CFOSAT). Based on the remarkable swell fields correlations emphasized by the present study, an effective assimilation system of swell observations in wave models is expected to be developed.

[62] Swells are today the most poorly predicted part of the sea state [Ardhuin *et al.*, 2008, 2010], with detrimental impact on delicate marine operations and, unfortunately, accidents due to heavy swells on the coast. Several assimilation methods have been imagined to improve wave forecasts [Voorrips *et al.*, 1997; Pinto *et al.*, 2005; Aouf *et al.*, 2006a] with, so far, very limited practical benefits [Bidlot *et al.*, 2007; Bidlot, 2008]. Exploiting the very large correlation scales of the swell field highlighted in the present study should help pushing further the time horizon of the assimilation impact.

[63] **Acknowledgments.** SAR data were provided by the European Space Agency (ESA). This work is a contribution to the ANR-funded project HEXECO, preparatory work for the China-France Ocean Satellite (CFOSAT), funded by CNES, and FP7-ERC project IOWAGA. Wave data were kindly provided by NOAA/NDBC through the website <http://www.ndbc.noaa.gov>. Model output used for the analysis is part of the IOWAGA database, available at <http://www.tinyurl.com/yetsofy>. This includes 8 year global and regional hindcast, with parameters describing the five most energetic swell partitions.

## References

- Aarnes, J. E. and H. E. Krogstad (2001), Partitioning sequences for the dissection of directional ocean wave spectra: A review, technical report, SINTEF Appl. Math., Oslo.
- Alves, J.-H. G. (2006), Numerical modeling of ocean swell contributions to the global wind-wave climate, *Ocean Modell.*, *11*, 98–122.
- Aouf, L., J.-M. Lefèvre, and D. Hauser (2006a), Assimilation of directional wave spectra in the wave model wam: An impact study from synthetic observations in preparation for the swimsat satellite mission, *J. Atmos. Oceanic Technol.*, *23*(3), 448–463.
- Aouf, L., J.-M. Lefèvre, D. Hauser, and B. Chapron (2006b), On the combined assimilation of RA-2 altimeter and ASAR wave data for the improvement of wave forecasting, paper presented at 15 Years of Progress in Radar Altimetry Symposium, Eur. Space Agency, Venice, Italy, 13–18 Mar.
- Ardhuin, F., F. Collard, B. Chapron, P. Queffelec, J.-F. Filipot, and M. Hamon (2008), Spectral wave dissipation based on observations: A global validation, paper presented at Chinese-German Joint Symposium on Hydraulics and Ocean Engineering, Ger. Fed. Minist. of Educ. and Res., Nat. Sci. Found. of China, Darmstadt, Germany, 25–26 Aug.
- Ardhuin, F., B. Chapron, and F. Collard (2009a), Observation of swell dissipation across oceans, *Geophys. Res. Lett.*, *36*, L06607, doi:10.1029/2008GL037030.
- Ardhuin, F., L. Marié, N. Rasclé, P. Forget, and A. Roland (2009b), Observation and estimation of Lagrangian, Stokes and Eulerian currents

- induced by wind and waves at the sea surface, *J. Phys. Oceanogr.*, **39**, 2820–2838.
- Ardhuin, F., et al. (2010), Semiempirical dissipation source functions for wind-wave models. Part I: Definition, calibration and validation, *J. Phys. Oceanogr.*, **40**, 1917–1941.
- Barber, N. F., and F. Ursell (1948), The generation and propagation of ocean waves and swell. Part I. Wave periods and velocities, *Phil. Trans. R. Soc. London A*, **240**, 527–560.
- Bernard, P. (1937), Relation entre la houle sur la côte nord du Maroc et l'agitation microsismique en Europe occidentale, *C. R. Acad. Sci. Paris*, **205**, 163–165.
- Bidlot, J.-R. (2008), Intercomparison of operational wave forecasting systems against buoys: Data from ECMWF, MetOffice, FNMOC, NCEP, DWD, BoM, SHOM and JMA, September 2008 to November 2008, technical report, *Jt. Tech. Comm. for Oceanogr. and Mar. Meteorol.*, World Meteorol. Organ., Intergov. Oceanogr. Comm., Geneva, Switzerland. (Available at [http://www.jcomm-services.org/modules/documents/documents/model\\_comparison\\_second\\_list\\_200809\\_200811.pdf](http://www.jcomm-services.org/modules/documents/documents/model_comparison_second_list_200809_200811.pdf).)
- Bidlot, J.-R., et al. (2007), Inter-comparison of operational wave forecasting systems, paper presented at 10th International Workshop of Wave Hindcasting and Forecasting, Coastal and Hydraul. Lab., U.S. Army Eng. Res. and Dev. Cent., North Shore, Hawaii, 11–16 Nov.
- Bromirski, P. D., R. E. Flick, and N. Graham (1999), Ocean wave height determined from inland seismometer data: Implications for investigating wave climate changes in the NE Pacific, *J. Geophys. Res.*, **104**, 20,753–20,766.
- Chapron, B., H. Johnsen, and R. Garello (2001), Wave and wind retrieval from SAR images of the ocean, *Ann. Telecommun.*, **56**, 682–699.
- Collard, F., F. Ardhuin, and B. Chapron (2009), Monitoring and analysis of ocean swell fields from space: New methods for routine observations, *J. Geophys. Res.*, **114**, C07023, doi:10.1029/2008JC005215.
- Gain, L. (1918), La prédiction des houles au Maroc, *Ann. Hydrogr.*, 65–75.
- Gelci, R., and H. Cazalé (1953), Une théorie énergétique de la houle appliquée au Maroc, *C. R. Soc. Sci. Nat. Phys. Maroc*, **(4)**, 64–66.
- Gelci, R., H. Cazalé, and J. Vassal (1957), Prédiction de la houle. La méthode des densités spectroangulaires, *Bull. Inf. Com. Oceanogr. Etude Cotes*, **9**, 416–435.
- Gerling, T. W. (1992), Partitioning sequences and arrays of directional ocean wave spectra into component wave systems, *J. Atmos. Oceanic Technol.*, **9**, 444–458.
- Gjevik, B., H. E. Korgstad, A. Lygre, and O. Rygg (1988), Long period swell wave events on the Norwegian shelf, *J. Phys. Oceanogr.*, **18**, 724–737.
- Greenslade, D. J. M., and I. R. Young (2005), The impact of altimeter sampling patterns on estimates of background errors in a global wave model, *J. Atmos. Oceanic Technol.*, **22**, 1895–1917.
- Hanson, J. L., and O. M. Phillips (2001), Automated analysis of ocean surface directional wave spectra, *J. Atmos. Oceanic Technol.*, **18**, 277–293.
- Hasselmann, S., C. Brüning, and K. Hasselmann (1996), An improved algorithm for the retrieval of ocean wave spectra from synthetic aperture radar image spectra, *J. Geophys. Res.*, **101**, 16,615–16,629.
- Johnsen, H., and F. Collard (2004), ASAR wave mode processing—Validation of reprocessing upgrade, *Tech. Rep. 168*, North. Res. Inst., Tromsø, Norway.
- Kedar, S., M. Longuet-Higgins, F. W. N. Graham, R. Clayton, and C. Jones (2008), The origin of deep ocean microseisms in the North Atlantic Ocean, *Proc. R. Soc. London A*, **464**, 1–35, doi:10.1098/rspa.2007.0277.
- Montagne, R. (1922), Le service de prédiction de la houle au Maroc, *Ann. Hydrogr.*, 157–186.
- Munk, W. H., G. R. Miller, F. E. Snodgrass, and N. F. Barber (1963), Directional recording of swell from distant storms, *Phil. Trans. R. Soc. London A*, **255**, 505–584.
- Pinto, J. P., M. C. Bernardino, and A. P. Silva (2005), A Kalman filter application to a spectral wave model, *Nonlinear Proc. Geophys.*, **12**, 775–782.
- Portilla, J., F. O. Torres, and J. Monbaliu (2009), Spectral partitioning and identification of wind sea and swell, *J. Atmos. Oceanic Technol.*, **26**, 107–122.
- Snodgrass, F. E., G. W. Groves, K. Hasselmann, G. R. Miller, W. H. Munk, and W. H. Powers (1966), Propagation of ocean swell across the Pacific, *Phil. Trans. R. Soc. London A*, **249**, 431–497.
- Sverdrup, H. U., and W. H. Munk (1947), Wind, sea, and swell: theory of relations for forecasting, *Tech. Rep. 601*, U.S. Hydrogr. Off., Washington, D. C.
- Tolman, H. L. (2002), Alleviating the garden sprinkler effect in wind wave models, *Ocean Modell.*, **4**, 269–289.
- Tolman, H. L. (2003), Treatment of unresolved islands and ice in wind wave models, *Ocean Modell.*, **5**, 219–231.
- Tolman, H. L. (2007), Automated grid generation for WAVEWATCH-III, *Tech. Rep. 254*, Environ. Canada, Toronto, Ont., Canada.
- Tolman, H. L. (2008), A mosaic approach to wind wave modeling, *Ocean Modell.*, **25**, 35–47, doi:10.1016/j.ocemod.2008.06.005.
- Tolman, H. L. (2009), User manual and system documentation of WAVEWATCH-III™ version 3.14, *Tech. Rep. 276*, NOAA/NWS/NCEP/MMAB.
- Tournadre, J. (1993), Time and space scales of significant wave heights, *J. Geophys. Res.*, **98**, 4727–4738.
- Ursell, F. (1999), Reminiscences of the early days of the spectrum of ocean waves, in *Wind-Over-Wave Couplings*, edited by S. G. Sajjadi, N. H. Thomas, and J. C. R. Hunt, pp. 127–137, Clarendon, Oxford, U. K.
- Voorrips, A. C., V. K. Makin, and S. Hasselmann (1997), Assimilation of wave spectra from pitch-and-roll buoys in a North Sea wave model, *J. Geophys. Res.*, **102**, 5829–5849.
- Wingert, K. M., T. H. C. Herbers, P. Wittman, and H. L. Tolman (2001), Validation Of operational global wave prediction models with spectral buoy data, paper presented at 4th International Symposium Ocean Wave Measurement and Analysis, Coasts, Oceans, Ports, and River Inst., San Francisco, Calif., 2–6 Sep.

F. Ardhuin and M. Delpy, Service Hydrographique et Oceanographique de la Marine, 13 rue du Chatellier, F-29200 Brest, France. (ardhuin@ifremer.fr; m.delpy@gmail.com)

B. Chapron, Laboratoire d'Océanographie Spatiale, Ifremer, Z.I. Centre de Brest, B.P. 70, F-29280 Plouzane, France. (bertrand.chapron@ifremer.fr)

F. Collard, Division Radar, Collecte Localisation Satellites, Batiment Ponant, Avenue la Perouse, Technopole Brest Iroise, F-29280 Plouzane, France. (dr.fab@cls.fr)